NANO LETTERS

pubs.acs.org/NanoLett
Letter

Quantum Sensitive, Record Dynamic Range Terahertz Tunnel Field-Effect Transistor Detectors Exploiting Multilayer Graphene/hBN/Bilayer Graphene/hBN Heterostructures

Leonardo Viti,* Lili Shi, Kenji Watanabe, Takashi Taniguchi, and Miriam S. Vitiello*

Cite This: *Nano Lett.* 2025, 25, 6005−6012

ABSTRACT: Sensitive photodetectors showing large quantum efficiencies and broad dynamic ranges are essential components for on-chip integrated photonic quantum platforms and for probing quantum correlations in metrological sources. However, at terahertz (THz) frequencies, this is a very challenging task owing to the lack of high-absorption materials and thermal effects that impact their noise figure. Here, we develop antenna-coupled tunnel field-effect transistors, based on multilayer graphene/hBN/bilayer graphene/hBN that detect multiwavelength beams at frequencies ∼3 THz with record performances. We reach noise-equivalent powers of $\sim 10^{-12}$ $WHz^{-1/2}$, a power dynamic range exceeding 5 orders of magnitude, limited by the maximum output power (0.8 mW) of the employed source, and a minimum detectable power at the nW-level, in a frequency-scalable device architecture. Our results open intriguing perspectives for the statistical analysis of quantum intensity correlations in nonclassical light sources operating in the underexploited THz frequency gap, between technologically mature domains (microwave, visible, near-infrared) that currently dominate the field of quantum technologies.

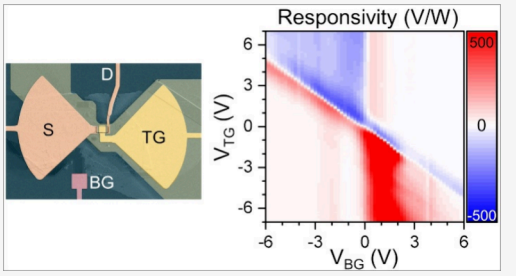

KEYWORDS: *Quantum detectors, terahertz, graphene, scalable nanodevices*

The quest for far-infrared (FIR) (1−15 THz) photodetectors providing quantum enhanced sensitivity and high saturation intensities (>1 W/cm^2) is currently driving extensive research efforts in astronomy,[1] spectroscopy,[2] and quantum information.[3] Traditional technological platforms, such as cryogenically cooled radiation detectors, have been dominant for decades. These detectors primarily rely on superconducting hot electron bolometers (HEBs),[4] superconducting transition-edge sensors (TESs),[5] and kinetic inductance detectors (KIDs),[6−8] operating at sub-Kelvin temperatures. These technologies have evolved over time, achieving the astrophysical photon noise limit, with a noise equivalent power (NEP, power required to obtain a unitary signal-to-noise ratio) as low as 10^{-20} $WHz^{-1/2}$.[9] As a result of these advancements, photon counting in the terahertz (THz) frequency range has become possible,[10] and the demonstration of single THz photon detection has been recently reported, in a narrow band, around 1.5 THz, using quantum capacitance detectors (QCDs).[11]

Alongside these established technologies, new material platforms and innovative device concepts have been proposed to address the challenge of sensitive photodetection, mostly at high (>3 THz) frequencies. For example, two-dimensional (2D) graphene has been recently used to realize a HEB based on a superconductor−graphene−superconductor (SGS) junction,[12] achieving NEP ≈ 3×10^{-20} $WHz^{-1/2}$. Furthermore, atomically thin layered van der Waals materials offer the possibility of being assembled with layer-by-layer control, enabling the realization of layered material heterostructures (LMHs) with novel and distinctive functionalities.[13] Specifically, controlling the twist angle between consecutive graphene layers (their relative crystallographic orientations) allows for the realization of twisted-magic-angle bilayer graphene (BLG), which exhibits superconducting behavior. This property has been leveraged in the development of ultrasensitive THz nanocalorimeters.[14]

A challenge in developing FIR photodetectors is achieving both high sensitivity (low NEP) and a large dynamic range. The operation of superconductor-based devices is typically limited to optical powers of ∼100 pW due to radiation-induced saturation.[15] This limitation can hinder their use in applications where photon statistics are measured, for instance, in the evaluation of quantum intensity correlations between optical modes,[16] or in the detection of squeezed states of light.[17]

Received: October 7, 2024
Revised: November 13, 2024
Accepted: November 14, 2024
Published: April 4, 2025

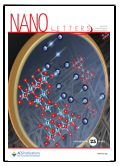

https://doi.org/10.1021/acs.nanolett.4c04934
Nano Lett. 2025, 25, 6005−6012

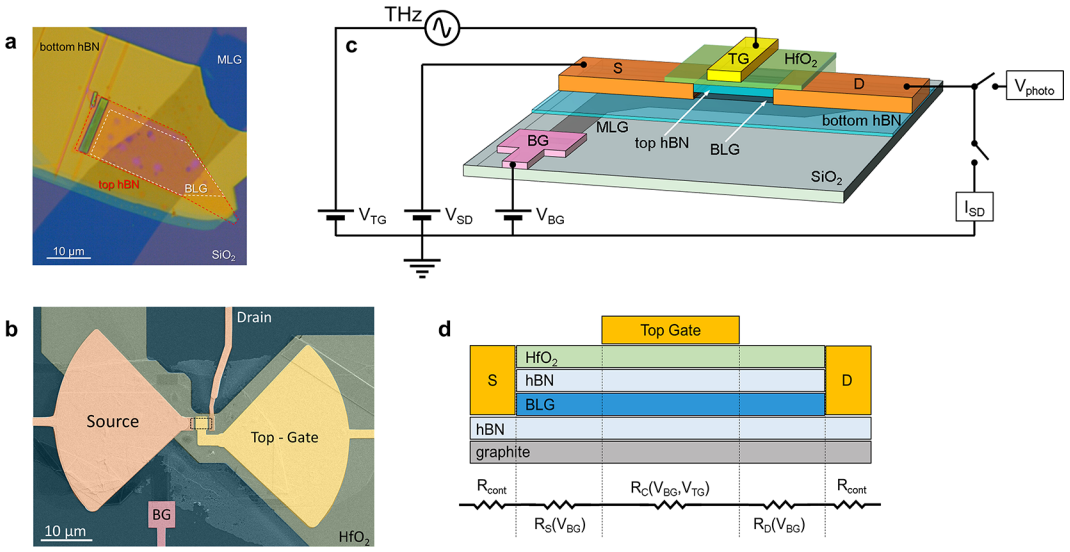

Figure 1. (a) Optical microscope image of the assembled layered materials heterostructure. The top-hBN flake is 15 nm thick, and the bottom hBN flake is 40 nm thick. (b) False color SEM image of the devised TFET. The bow-tie antenna is connected to the source and top-gate electrodes. (c) Schematic diagram of the BLG−FET active element, indicating the different materials composing the device and the electrical scheme adopted for electrical and optical characterizations. The gating scheme is indicated on the left-hand side. (d) Schematic longitudinal cross-section of the active element, showing five different regions along the BLG channel, which can be described as a series of resistors. The S and D contacts have intrinsic contact resistance (R_{cont}). The regions not covered by the top-gate are only influenced by the MLG bottom-gate with resistances R_S and R_D at the source and drain sides, respectively. The resistance of the central region (R_C) is influenced by the combined action of the two gates.

Interestingly, 2D materials may provide a valuable solution in this respect. In particular, photodetectors based on single-layer graphene (SLG) and bilayer graphene (BLG) have shown large dynamic ranges (up to 4 orders of magnitude)[18−20] due to their high saturation currents and efficient electron cooling dynamics (electron-optical phonon scattering time of ∼1 ps[21,22]).

Additionally, BLG, which is a gapless semiconductor in its pristine form, allows for the induction and tuning of an energy gap (E_g) in its band structure through interaction with a substrate[23] or by applying an external out-of-plane electric field.[24] This field can be generated, for example, by breaking the out-of-plane inversion symmetry with a neighboring crystal, inducing a finite E_g by proximity. This crystal field has been used to activate a THz gap (E_g = 10 meV[25]) in large-twist-angle double BLG heterostructures, leading to the development of ultrabroadband photovoltaic detectors with a frequency coverage spanning from the THz to the near-infrared range.[26]

Importantly, the bandgap of BLG can also be adjusted by an out-of-plane electric field, controlled by external dual-gate electrodes.[27,28] This configuration has been used to realize tunnel field-effect transistors (TFETs) based on BLG, which operate as sensitive photodetectors (NEP ≈ 30−300 × 10^{-15} $WHz^{-1/2}$) at frequencies around 100 GHz in single-top-gated[29] or top p−n junction[30,31] configurations.

Here, we propose to employ TFETs as a technological approach for quantum-sensitive THz receivers targeting frequencies (3 THz) higher than those reported in previous works,[29−31] where a sensitivity drop typically occurs. By selecting BLG as the core active material, we demonstrate the powerful and broadband capability of the TFET device concept, in a spectral range never addressed so far, and with state of the art performances.

The proposed photodetector comprises a multilayer graphene (MLG)/hexagonal boron nitride (hBN)/BLG/hBN heterostructure and exploits the tunability of the energy gap of BLG to create a lateral tunnel junction between the gated and ungated portions of the BLG−FET channel. By exploiting the junction nonlinearity, it rectifies the incoming THz radiation. The subwavelength TFET channel is coupled to the impinging radiation via a planar bow-tie antenna, specifically designed to be resonant at 3 THz. Remarkably, the proposed concept is frequency scalable, from 0.1 to 10 THz, across the entire sub-THz and FIR ranges. Importantly, in our geometry, the antenna is asymmetrically coupled to the source (S) and top-gate (TG) electrodes, enabling zero-bias operation of the tunnel-junction rectifier.

The demonstrated capability of TFETs to operate as quantum sensitive photodetectors at frequencies of ∼3 THz, combined with the inherent frequency scalability of this device concept, offers concrete perspectives for detecting nonclassical states of THz light that could be generated by THz quantum cascade laser (QCL) frequency combs. This opens up exciting opportunities for developing THz quantum platforms based on solid-state devices. A state-of-the-art combination of performances is demonstrated, achieving a minimum NEP of 10^{-12} $WHz^{-1/2}$ and a dynamic range exceeding 5 orders of magnitude, limited by the maximum output power (0.8 mW) of the employed QCL source.

All flakes used for the MLG/hBN/BLG/hBN heterostructure assembly are mechanically exfoliated from bulk crystals (Supporting Information). In order to implement a dual-gated architecture, we positioned BLG, encapsulated in hBN, on a thin MLG (8−10 layers) flake, which serves as back-gate (BG) electrode. hBN−BLG−hBN heterostructures are assembled using a standard dry-transfer technique,[32,33] as described in the Supporting Information. An optical image of one of the assembled LMHs, transferred onto a Si/SiO_2 substrate, is shown in Figure 1a. After the LMH assembly, the antenna-coupled BLG-FETs are fabricated following the procedure described in the Supporting Information. Figure 1b displays a

https://doi.org/10.1021/acs.nanolett.4c04934
Nano Lett. 2025, 25, 6005−6012

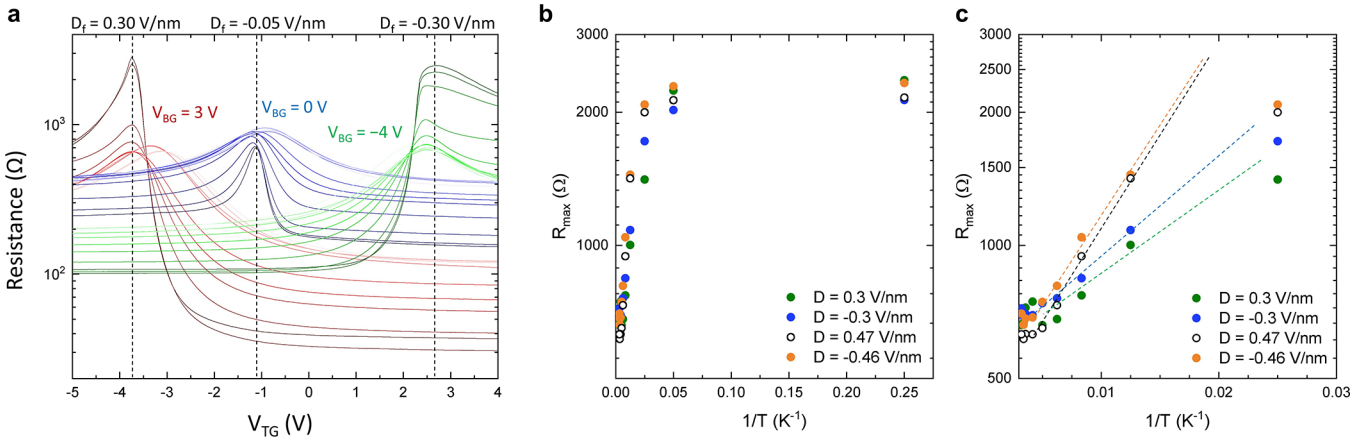

Figure 2. (a) Isotherm curves showing channel resistance of S#2 as a function of top-gate voltage (V_{TG}), acquired at three different values of V_{BG}: +3 V (red lines), 0 V (blue lines), and −4 V (green lines). The curves for two additional values of V_{BG} (−6 V and +5 V) are reported in the Supporting Information. The temperature is changed from 4 K (darker lines) to 310 K (brighter lines), sweeping through the values (4, 20, 40, 80, 120, 160, 200, 240, 280, 294, and 310 K). The vertical dashed lines indicate specific values of the displacement field (D), which is responsible of the bandgap opening in BLG. Since the contact resistance (R_{cont}) changes as a function of temperature (see Supporting Information), its value has been subtracted from the data in (a). (b) Scatter plot of the resistance peak as a function of the inverse of the temperature (Arrhenius plot) evaluated at four different values of the displacement field (D_f). (c) Zoom of the graph in (b) in the region of temperatures where the slope of $\ln(R_{max})$ vs 1/T is linear (40 K: 200 K). In this region, we apply a linear fit to $\ln(R_{max})$ to evaluate the energy gap.

false-color scanning electron microscope (SEM) picture of one of the investigated devices. The BLG−FET channel is shaped as a rectangle, with length L_c = 6 μm and width W_c = 3 μm, and is connected to the source (S) and drain (D) electrodes. The top-gate (TG) electrode is electrically isolated from the BLG channel by the top-hBN flake and a 30 nm thick layer of HfO_2 grown by atomic layer deposition (ALD). The THz bow-tie antenna has a radius of 21 μm, set to be resonant with 3 THz radiation.[34] These dimensions are selected following the results of electromagnetic simulations performed with a commercial software (COMSOL Multiphysics[35]), based on a finite elements method. This system configuration entails a relatively simple device circuitry, as shown schematically in Figure 1c: two hardware switches enable the selection between electrical and optical characterization experiments. We study two devices, S#1 and S#2. A description of their geometrical parameters is reported in the Supporting Information.

To investigate the performance of the photodetector at low temperatures, we mounted the device in a He flow cryostat (Janis Research) with THz optical access and controllable heat-sink temperature (T) between 4.2 and 300 K (room temperature, RT). To ensure effective thermal contact between the cryostat's copper cold unit and the silicon substrate, the sample is soldered onto a copper-carrier using an indium-based soldering alloy (Indium Corporation, PTI290/84/F).

We examine the impact of vertical electrostatic gating on the BLG bandgap by studying electron transport through the BLG-channel at cryogenic temperatures. This electrical characterization is performed by independently controlling the source−drain bias (V_{SD}), the back-gate voltage (V_{BG}), and the top-gate voltage (V_{TG}), and measuring the current at the D electrode (I_{SD}) using *dc* source meters (Keithley, SMU-K2400). The dependence of the two-terminal channel resistance (R) on V_{TG}, measured at various T values for sample S#2, and at different V_{BG}, is shown in Figure 2a. The transport is strongly affected by the out-of-plane displacement field (D_f), which increases when the top- and back-gates have opposite polarities (see Supporting Information). In particular, for $|D_f|$ > 0.3 V/nm, the maximum value of R (R_{max}) consistently increases as T decreases from 200 to 4.2 K, indicating a gap opening.[36] By analyzing the temperature dependence of R_{max}, it is possible to quantitatively estimate the energy gap of BLG. The $R_{max}(1/T)$ trend reveals an activation behavior (Figure 2b,c) that follows an Arrhenius-type dependence: $R_{max} = R_0 + \exp(E_g/2k_BT)$, where k_B is the Boltzmann constant. By conducting a linear fit to the Arrhenius plots in the temperature range between 40 and 200 K, we estimate E_g = 7.2 meV for D_f = 0.3 V/nm, E_g = 8.5 meV for D_f = −0.3 V/nm, E_g = 15.5 meV for D_f = 0.47 V/nm, and E_g = 17.4 meV for D_f = −0.46 V/nm, confirming the presence of a gate-tunable bandgap in the BLG channel (data for $|D_f|$ > 0.4 V/nm are shown in the Supporting Information). We note that the estimated E_g values are a factor of ∼2 smaller than those expected for ultraclean BLG heterostructures at similar $|D_f|$ values.[37,38] The observed discrepancy indicates the presence of disorder-induced subgap states.[38]

We test the THz photoresponse performance of the TFET using a focused beam generated by a 3 THz QCL. This allows us to tune the average optical power (P_t) at the detector position up to ∼0.8 mW (see Supporting Information). The THz beam, polarized parallel to the TFET antenna axis, is focused by using two lenses. For optical characterization, the TFET photovoltage (V_{photo}, Figure 1c) is measured at the D electrode using a lock-in amplifier (SR5210) after preamplification (dLInstruments, model 1201, gain g = 1000). In order to reduce the 1/f contribution to the detector's noise figure,[39] we electrically modulate the intensity of the QCL with a square-wave envelope at a frequency of 7.333 kHz.

We used BLG-TFET to measure the intensity distribution in the focal xy plane. Figure 3a shows the intensity profile as a map of V_{photo} when P_t = 100 μW. The visible Airy pattern demonstrates the good sensitivity of the photodetector. We calculate the beam spot area S_t as the area of an ellipse with major and minor axes given by the half-width at half-maximum (HWHM) of the beam profiles along the x and y directions (dashed lines in Figure 3a).

We obtain $S_t = 80 \times 10^{-3}$ mm^2. Since the detector's active area is much smaller than S_t, we estimate the fraction of optical power impinging on the TFET as $P_a = (P_t{*}t) \times (S_\lambda/S_t)$, where

https://doi.org/10.1021/acs.nanolett.4c04934
Nano Lett. 2025, 25, 6005−6012

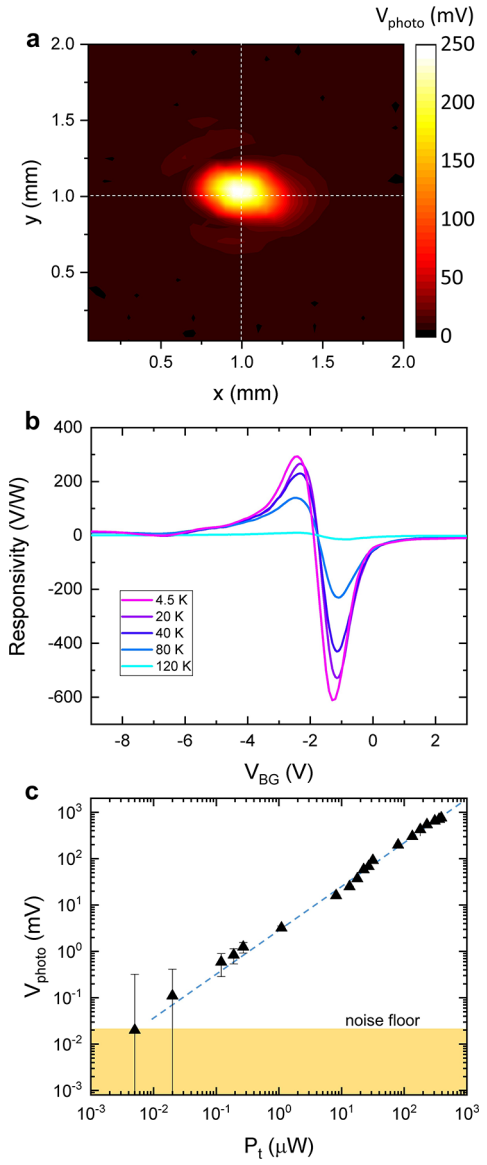

Figure 3. (a) Lock-in signal (V_{photo}) measured by the TFET in the focal plane, for P_t = 100 μW and T = 4.5 K. The 2 × 2 mm^2 map is acquired by translating the optical cryostat using a heavy duty *xy* mechanical stage (Physik Instrumente, LS180). The profiles at the center of the beam (dashed lines) give beam waists of 400 and 250 μm along the *x* and *y* directions, respectively. (b) Responsivity curves measured as a function of V_{BG}, obtained at various operating temperatures. (c) Low-temperature V_{photo} plotted as a function of P_t in log−log scale, with V_{BG} = −1 V and V_{TG} = 0 V. The dashed line represents a linear fit to the data. The shaded area represents the experimental noise floor (~20 μV) on the lock-in amplifier. The error bars indicate the amplitude of the background signal (THz light off) summed to the root-mean-square deviation of the measured photovoltage.

t = 0.5 represents the transmittance through the high-density polyethylene (HDPE) cryostat window, $S_\lambda = \lambda^2/4$ represents the diffraction-limited area[40] (see Supporting Information), and the value of the ratio S_t/S_λ is approximately 50. We then evaluate the voltage responsivity using the expression:[20,41]

$$R_v = \frac{2\sqrt{2}\,(\pi/4)}{g} \times \frac{V_{photo}}{P_a} \quad (1)$$

where the factor 2 accounts for the peak-to-peak magnitude, $\sqrt{2}$ originates from the root means square amplitude of the lock-in amplifier, and $\pi/4$ represents the fundamental sine wave Fourier component of the square-wave produced by the square-wave envelope used to modulate the QCL.

Figure 3b shows the plot of $R_v(V_{BG})$ acquired at various temperatures for sample S#1. The responsivity increases as T is lowered, as a result of the sharper nonlinearity in the channel resistance (see Supporting Information).[29] It reaches a maximum value of approximately 0.6 kV/W near the CNP for T = 4.5 K. We note that in this measurement, the top-gate voltage is not employed, V_{TG} = 0 V; thus, the displacement field weakly departs from zero, and the photoresponse is dominated by the resistive self-mixing effect, as discussed in detail in the Supporting Information.

We then characterize the dynamic range of the detector by sweeping the QCL power from zero to P_t = 800 μW. The TFET can detect a minimum optical power of ~5 nW (through the cryostat window) and its response is nearly linear over the entire range of investigated powers, showing a close to unity power-dependence $V_{photo} \approx P_t^{\gamma}$, with γ = 0.96 (Figure 3c). It is worth noting that the high-power limit of the dynamic range for the investigated BLG-TFET detector is determined by the maximum power of the QCL, which represents an intrinsic limitation of our experimental setup.

To investigate how the electrical transport and photoresponse are influenced by the combined action of the two gates, we map I_{SD} and the responsivity as a function of V_{TG} and V_{BG}. The transport map shown in Figure 4a, relative to sample S#1, reveals two minima, corresponding to two distinct CNPs: a fixed one (CNP_1), described by a vertical line at $V_{BG} \approx -1.5$ V, and a top-gate-tunable one (CNP_2), represented by a diagonal line. We attribute the presence of these two CNPs to the existence of two distinct regions along the BLG channel. Indeed, in our geometry, the top-gate electrode is narrower than the bottom gate, which acts on the BLG regions near the S and D contacts (Figure 1d). These regions are not affected by V_{TG}, and their transport tunability by V_{BG} is proven by CNP_1. Conversely, the diagonal line marks the shift of CNP_2 under the simultaneous influence of the two gates, in the double-gated region of BLG, with a slope determined by the ratio of the gate lever arms (see Supporting Information).[38] Based on this understanding, we can identify four distinct doping regions in the map of $I_{SD}(V_{BG},V_{TG})$: *n*−*p*, *n*−*n*, *p*−*n*, and *p*−*p*, with the first letter denoting the dual-gated area.

For sample S#1, a strong correspondence is visible between the $I_{SD}(V_{BG},V_{TG})$ and $R_v(V_{BG},V_{TG})$ maps (Figure 4a,b). A significantly larger photovoltage signal is observed when the *p*−*n* junction is active, whereas a much smaller signal is detected in other regions. Importantly, this responsivity pattern differs from what is typically observed in the photothermoelectric (PTE) effect, which would instead result in a 6-fold pattern.[19,31,42] Instead, the retrieved pattern aligns with those found in similar single-top-gate TFETs operating at lower excitation frequencies.[29] We note that for sample S#1, a small increase in resistance is visible when moving along the line marked by CNP2. This is related to the reduced bandgap opening effect under the influence of D_f, which we attribute to a inadequately clean LMH: residual impurities and defects can lead to the presence of disorder-induced subgap states.[38]

The situation is different for sample S#2, where R increases for larger displacement fields along the diagonal line CNP2 (Figure 4c), with I_{SD} changing by 2 orders of magnitude

https://doi.org/10.1021/acs.nanolett.4c04934
Nano Lett. 2025, 25, 6005−6012

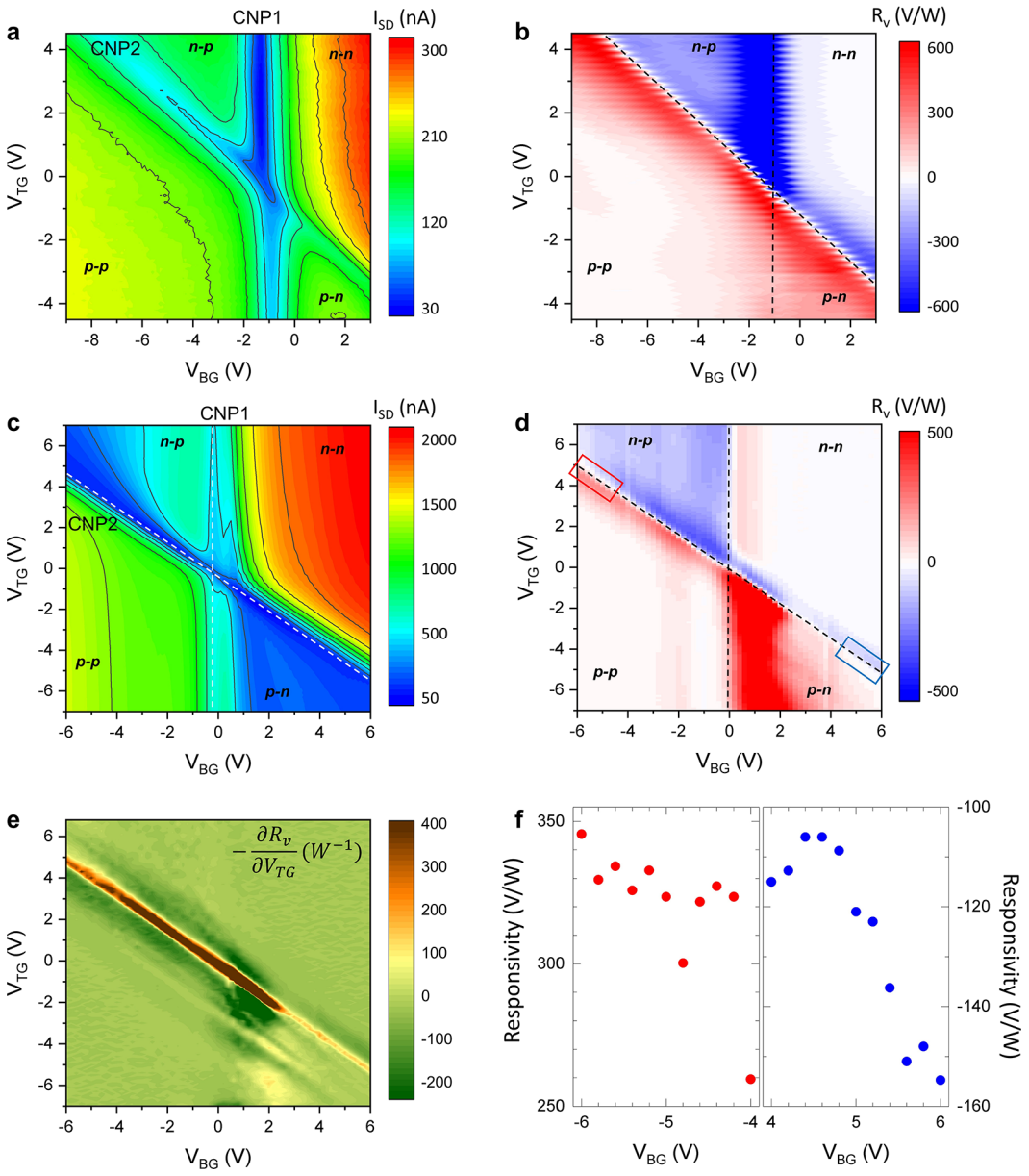

Figure 4. (a) S#1: electrical transport characterization at 4.5 K: I_{SD} map measured as a function of V_{BG} (span from −9 V to +3 V) and V_{TG} (span from −4.5 V to +4.5 V). Different junction configurations are highlighted (*p*−*p*, *n*−*p*, etc.). (b) S#1: voltage responsivity map measured as a function of V_{BG} and V_{TG}. (c) S#2: electrical transport characterization at 4.5 K: I_{SD} map measured as a function of V_{BG} (span from −6 V to +6 V) and V_{TG} (span from −7 V to +7 V). (d) S#2: $R_v(V_{BG},V_{TG})$. In this case, a 6-fold pattern appears, indicating a thermoelectric contribution to the photodetection. Colored boxes indicate regions at high displacement fields near CNP2. (e) Map of the first derivative of $R_v(V_{BG},V_{TG})$, with respect to V_{TG}. Oscillations are visible in the background, appearing as diagonal lines, almost parallel to the sign-change line at CNP2. (f) Maximum responsivity measured in the boxes in (d), plotted as a function of V_{BG}. R_v increases for larger displacement fields.

between different regions of the $I_{SD}(V_{BG},V_{TG})$ map. The $R_v(V_{BG},V_{TG})$ map shown in Figure 4d presents different features compared to those of device S#1. First, a 6-fold pattern is visible, indicating a photothermoelectric contribution to the response.[31,42] Second, distinctive features appear in the map, represented by faint diagonal lines, almost parallel to the main sign change along CNP2. These features clearly emerge in the map of the first derivative of R_v (Figure 4e) and can be linked to the excitation of plasmonic resonances in the gated BLG channel, in agreement with previous findings in high-quality SLG- and BLG-based THz detectors.[43,44] Importantly, R_v increases when gate voltages are swept along the CNP2 line, away from the map center, i.e., for increasing displacement fields (Figure 4f). This can be explained by the onset of tunnelling rectification, which is expected to increase for large D_f.[29] Therefore, we conclude that three rectification mechanisms contribute to the $R_v(V_{BG},V_{TG})$ map of S#2: photothermoelectric effect, plasmonic, and tunneling rectifications.

We eventually calculated the NEP of the BLG-TFETs. For this purpose, we assume that the noise spectral density (NSD), which is the amount of noise power per unit bandwidth, is primarily due to thermal fluctuations. This assumption is valid because of the high modulation frequency (7.333 kHz) used in our experiments.[36] Using the expression NEP = $1/R_v \times (4k_BRT)^{1/2}$,[39] and the values of R and R_v extracted from the maps in Figure 4a−d, we estimate a minimum NEP of 1.1 ×

https://doi.org/10.1021/acs.nanolett.4c04934
Nano Lett. 2025, 25, 6005−6012

10^{-12} $WHz^{-1/2}$ for S#1 and of 1.3×10^{-12} $WHz^{-1/2}$ for S#2. These values are not competitive with respect to the sensitivities of more established and technologically mature commercial devices, such as HEBs,[9] QCDs,[11] and KIDs,[8] exhibiting NEPs < 10^{-21} $WHz^{-1/2}$. However, the TFET device concept could serve as a complementary technological platform, allowing for less stringent cooling requirements and covering a range of input powers (above ∼100 fW[31]) that are not accessible with superconductor-based devices. Indeed, HEBs show typical saturation powers of ∼10 pW−100 pW (depending on the absorbing element dimensions), QCDs operate within a power range of 10^{-22} W to 10^{-15} W,[11] and KIDs exhibit a dynamic range from ∼100 zW to ∼100 fW.[8] In particular, the large dynamic range (>5 orders of magnitude) demonstrated in this work, combined with an almost linear dependence of the photoresponse on input intensity, makes the proposed TFETs a suitable direct detector system for measuring intensity correlations between high-fluence optical modes at frequencies of ∼3 THz.

We have conceived and devised THz frequency quantum detectors based on MLG/hBN/BLG/hBN heterostructures embedded in a TFET architecture, operating as sensitive photodetectors at ∼3 THz, with a wide and setup-limited dynamic range exceeding 5 orders of magnitude. The retrieved NEP is ∼10^{-12} $WHz^{-1/2}$, with a minimum detectable power at the nW level. The design is frequency scalable across the entire 2−4.5 THz range of available quantum laser sources, e.g., miniaturized frequency combs, and suitable to be combined on-chip with coplanar striplines and bandpass filters, potentially pushing their speed limit at the sub-ns level.[42] We envision several design strategies to further enhance the performance of this study. For example, using a double-top-gate geometry allows for the creation of an additional $p-n$ junction at the center of the BLG channel, inducing a strong and bandgap-tunable PTE response, which can increase the sensitivity of the detector by approximately five times compared to the single-top-gate scheme.[31] Implementing a better optical coupling scheme, such as silicon lens coupling, could also improve the responsivity. Additionally, it is noteworthy that BLG is progressively becoming a mature material platform, with the potential of synthesis through low pressure chemical vapor deposition (LP-CVD)[36] and integration into high-quality LMHs.[45] This advancement could shift BLG-TFET technology from laboratory-based fabrications and experiments to a more technologically mature domain, opening up perspectives for extensive use in the fields of FIR quantum optics and quantum communications.

■ ASSOCIATED CONTENT

Data Availability Statement

The data that support the plots within this paper and other finding of this study are available from the corresponding authors upon reasonable request.

Supporting Information

The Supporting Information is available free of charge at https://pubs.acs.org/doi/10.1021/acs.nanolett.4c04934.

Additional experimental details, materials, and methods, including: experimental details on device fabrication; additional details on the experimental setup for optical characterization; evaluation of the gate lever arms; evaluation of the displacement field; evaluation of electrical properties at different temperatures; resistance curves at higher displacement fields; sample-to-sample variability; resistive self-mixing photodetection; responsivity normalization (PDF)

Accession Codes

The codes and simulation files that support the plots and data analysis within this paper are available from the corresponding author upon reasonable request.

■ AUTHOR INFORMATION

Corresponding Authors

Miriam S. Vitiello − *NEST, CNR-NANO and Scuola Normale Superiore, 56127 Pisa, Italy;* orcid.org/0000-0002-4914-0421; Email: miriam.vitiello@sns.it

Leonardo Viti − *NEST, CNR-NANO and Scuola Normale Superiore, 56127 Pisa, Italy;* orcid.org/0000-0002-4844-2081; Email: leonardo.viti@nano.cnr.it

Authors

Lili Shi − *NEST, CNR-NANO and Scuola Normale Superiore, 56127 Pisa, Italy*

Kenji Watanabe − *National Institute for Materials Science, Tsukuba 305-0044, Japan;* orcid.org/0000-0003-3701-8119

Takashi Taniguchi − *National Institute for Materials Science, Tsukuba 305-0044, Japan;* orcid.org/0000-0002-1467-3105

Complete contact information is available at: https://pubs.acs.org/10.1021/acs.nanolett.4c04934

Notes

The authors declare no competing financial interest.

■ ACKNOWLEDGMENTS

This work was supported by the European Research Council through the ERC project Terascan (101157731), by the European Union under the Italian National Recovery and Resilience Plan (NRRP) of Next Generation EU, partnership on PE0000023-NQSTI), and by the European Union through the FET Open project EXTREME IR (944735).

■ REFERENCES

(1) de Graauw, T.; Helmich, F. P.; Phillips, T. G.; et al. The Herschel-Heterodyne Instrument for the Far-Infrared (HIFI). *A&A* **2010**, *518*, L6.

(2) Torrioli, G.; Forrer, A.; Beck, M.; Carelli, P.; Chiarello, F.; Faist, J.; Gaggero, A.; Giovine, E.; Martini, F.; Senica, U.; Leoni, R.; Scalari, G.; Cibella, S. THz optical beat-note detection with a fast superconducting hot electron bolometer operating up to 31 GHz. *Opt. Express* **2023**, *31*, 15942−15952.

(3) Todorov, Y.; Dhillon, S.; Mangeney, J. THz quantum gap: exploring potential approaches for generating and detecting non-classical states of THz light. *Nanophotonics* **2024**, *13*, 1681−1691.

(4) Shurakov, A.; Lobanov, Y.; Goltsman, G. Superconducting hot-electron bolometer: from the discovery of hot-electron phenomena to practical applications *Supercond. Sci. Technol.* **2016**, *29*, No. 023001.

(5) Irwin, K. D.; Hilton, G. C. Transition−edge sensors. In *Cryogenic Particle Detection*; Enss, C.; Springer: Berlin, 2005; pp 63−149.

(6) Day, P.; LeDuc, H.; Mazin, B.; Vayonakis, A.; Zmuidzinas, J. A broadband superconducting detector suitable for use in large arrays. *Nature* **2003**, *425*, 817−821.

(7) Mazin, B. A. Microwave kinetic inductance detectors: the first decade. *AIP Conf. Proc.* **2009**, *1185*, 135−142.

(8) Day, P. K.; Cothard, N. F.; Albert, C.; Foote, L.; Kane, E.; Eom, B. H.; Thakur, R. B.; Janssen, R. M. J.; Beyer, A.; Echternach, P.; van

Berkel, S.; Hailey-Dunsheath, S.; Stevenson, T. R.; Dabironezare, S.; Baselmans, J. J. A.; Glenn, J.; Bradford, C. M.; Leduc, H. G. A 25-micron single photon sensitive kinetic inductance detector. *Phys. Rev. X* **2024**, *14*, No. 041005.
(9) Rogalski, A. Semiconductor detectors and focal plane arrays for far-infrared imaging. *Opto-Electron. Rev.* **2013**, *21*, 406−426.
(10) Karasik, B. S.; Olaya, D.; Wei, J.; Pereverzev, S.; Gershenson, M. E.; Kawamura, J. H.; McGrath, W. R.; Sergeev, A. V. Record−low NEP in hot−electron titanium nanobolometers. *IEEE T. Appl. Supercon.* **2007**, *17*, 293−297.
(11) Echternach, P. M.; Pepper, B. J.; Reck, T.; Bradford, C. M. Single photon detection of 1.5 THz radiation with the quantum capacitance detector. *Nature. Astronomy* **2018**, *2*, 90−97.
(12) Kokkoniemi, R.; Girard, J.-P.; Hazra, D.; Laitinen, A.; Govenius, J.; Lake, R. E.; Sallinen, I.; Vesterinen, V.; Partanen, M.; Tan, J. Y.; Chan, K. W.; Tan, K. Y.; Hakonen, P.; Möttönen, M. Bolometer operating at the threshold for circuit quantum electrodynamics. *Nature* **2020**, *586*, 47−51.
(13) Geim, A.; Grigorieva, I. V. Van der Waals heterostructures. *Nature* **2013**, *499*, 419−425.
(14) Seifert, P.; Lu, X.; Stepanov, P.; Retamal, J. R. D.; Moore, J. N.; Fong, K. C.; Principi, A.; Efetov, D. K. Magic-Angle Bilayer Graphene Nanocalorimeters: Toward Broadband Energy-Resolving Single Photon Detection. *Nano Lett.* **2020**, *20*, 3459−3464.
(15) Kuzmin, L. S.; Pankratov, A. L.; Gordeeva, A. V.; Zbrozhek, V. O.; Shamporov, V. A.; Revin, L. S.; Blagodatkin, A. V.; Masi, S.; de Bernardis, P. Photon-noise-limited cold-electron bolometer based on strong electron self-cooling for high-performance cosmology missions. *Commun. Phys.* **2019**, *2*, 104.
(16) Gabbrielli, T.; Bruno, N.; Corrias, N.; Borri, S.; Consolino, L.; Bertrand, M.; Shahmohammadi, M.; Franckié, M.; Beck, M.; Faist, J.; Zavatta, A.; Cappelli, F.; De Natale, P. Intensity Correlations in Quantum Cascade Laser Harmonic Frequency Combs. *Adv. Photonics Res.* **2022**, *3*, 2200162.
(17) Andersen, U. L.; Gehring, T.; Marquardt, C.; Leuchs, G. 30 years of squeezed light generation. *Phys. Scr.* **2016**, *91*, 053001.
(18) Koppens, F. H. L.; Mueller, T.; Avouris, P.; Ferrari, A. C.; Vitiello, M. S.; Polini, M. Photodetectors based on graphene, other two-dimensional materials and hybrid systems. *Nat. Nanotechnol.* **2014**, *9*, 780−793.
(19) Castilla, S.; Terrés, B.; Autore, M.; Viti, L.; Li, J.; Nikitin, A. Y.; Vangelidis, I.; Watanabe, K.; Taniguchi, T.; Lidorikis, E.; Vitiello, M. S.; Hillenbrand, R.; Tielrooij, K.-J.; Koppens, F. H. L. Fast and Sensitive Terahertz Detection Using an Antenna-Integrated Graphene pn Junction. *Nano Lett.* **2019**, *19*, 2765.
(20) Viti, L.; Purdie, D. G.; Lombardo, A.; Ferrari, A. C.; Vitiello, M. S. HBN-Encapsulated, Graphene-based, Room-temperature Terahertz Receivers, with High Speed and Low Noise. *Nano Lett.* **2020**, *20*, 3169.
(21) Pogna, E. A. A.; Jia, X.; Principi, A.; Block, A.; Banszerus, L.; Zhang, J.; Liu, X.; Sohier, T.; Forti, S.; Soundarapandian, S.; Terrés, B.; Mehew, J. D.; Trovatello, C.; Coletti, C.; Koppens, F. H. L.; Bonn, M.; Wang, H. I.; van Hulst, N.; Verstraete, M. J.; Peng, H.; Liu, Z.; Stampfer, C.; Cerullo, G.; Tielrooij, K.-J. Hot-Carrier Cooling in High-Quality Graphene Is Intrinsically Limited by Optical Phonons. *ACS Nano* **2021**, *15*, 11285−11295.
(22) Massicotte, M.; Soavi, G.; Principi, A.; Tielrooij, K.-J. Hot carriers in graphene−fundamentals and applications. *Nanoscale* **2021**, *13*, 8376−8411.
(23) Hunt, B.; Sanchez-Yamagishi, J. D.; Young, A. F.; Yankowitz, M.; LeRoy, B. J.; Watanabe, K.; Taniguchi, T.; Moon, P.; Koshino, M.; Jarillo-Herrero, P.; Ashoori, R. C. Massive Dirac fermions and Hofstadter butterfly in a van der Waals heterostructure. *Science* **2013**, *340*, 1427−1430.
(24) Min, H.; Sahu, B.; Banerjee, S. K.; MacDonald, A. H. Ab initio theory of gate induced gaps in graphene bilayers. *Phys. Rev. B* **2007**, *75*, 155115.
(25) Rickhaus, P.; Zheng, G.; Lado, J. L.; Lee, Y.; Kurzmann, A.; Eich, M.; Pisoni, R.; Tong, C.; Garreis, R.; Gold, C.; Masseroni, M.; Taniguchi, T.; Wantanabe, K.; Ihn, T.; Ensslin, K. Gap Opening in Twisted Double Bilayer Graphene by Crystal Fields. *Nano Lett.* **2019**, *19*, 8821−8828.
(26) Agarwal, H.; Nowakowski, K.; Forrer, A.; Principi, A.; Bertini, R.; Batlle-Porro, S.; Reserbat-Plantey, A.; Prasad, P.; Vistoli, L.; Watanabe, K.; Taniguchi, T.; Bachtold, A.; Scalari, G.; Krishna Kumar, R.; Koppens, F. H. L. Ultra-broadband photoconductivity in twisted graphene heterostructures with large responsivity. *Nat. Photonics* **2023**, *17*, 1047−1053.
(27) Ohta, T.; Bostwick, A.; Seyller, T.; Horn, K.; Rotenberg, E. Controlling the electronic structure of bilayer graphene. *Science* **2006**, *313*, 951−954.
(28) Zhang, Y.; Tang, T.-T.; Girit, C.; Hao, Z.; Martin, M. C.; Zettl, A.; Crommie, M. F.; Shen, Y. R.; Wang, F. Direct observation of a widely tunable bandgap in bilayer graphene. *Nature* **2009**, *459*, 820−823.
(29) Gayduchenko, I.; Xu, S. G.; Alymov, G.; Moskotin, M.; Tretyakov, I.; Taniguchi, T.; Watanabe, K.; Goltsman, G.; Geim, A. K.; Fedorov, G.; Svintsov, D.; Bandurin, D. A. Tunnel field-effect transistors for sensitive terahertz detection. *Nat. Commun.* **2021**, *12*, 543.
(30) Mylnikov, D. A.; Titova, E. I.; Kashchenko, M. A.; Safonov, I. V.; Zhukov, S. S.; Semkin, V. A.; Novoselov, K. S.; Bandurin, D. A.; Svintsov, D. A. Terahertz Photoconductivity in Bilayer Graphene-Transistors: Evidence for Tunneling at Gate-Induced Junctions. *Nano Lett.* **2023**, *23*, 220−226.
(31) Titova, E.; Mylnikov, D.; Kashchenko, M.; Safonov, I.; Zhukov, S.; Dzhikirba, K.; Novoselov, K. S.; Bandurin, D. A.; Alymov, G.; Svintsov, D. Ultralow-noise Terahertz Detection by p−n Junctions in Gapped Bilayer Graphene. *ACS Nano* **2023**, *17*, 8223−8232.
(32) Pizzocchero, F.; Gammelgaard, L.; Jessen, B.; Caridad, J. M.; Wang, L.; Hone, J.; Boggild, P.; Booth, T. J. The hot pick-up technique for batch assembly of van der Waals heterostructures. *Nat. Commun.* **2016**, *7*, 11894.
(33) Purdie, D. G.; Pugno, N. M.; Taniguchi, T.; Watanabe, K.; Ferrari, A. C.; Lombardo, A. Cleaning interfaces in layered materials heterostructures. *Nat. Commun.* **2018**, *9*, 5387.
(34) Asgari, M.; Riccardi, E.; Balci, O.; De Fazio, D.; Shinde, S. M.; Zhang, J.; Mignuzzi, S.; Koppens, F. H. L.; Ferrari, A. C.; Viti, L.; Vitiello, M. S. Chip-Scalable, Room-Temperature, Zero-Bias, Graphene-Based Terahertz Detectors with Nanosecond Response Time. *ACS Nano* **2021**, *15*, 17966−17976.
(35) COMSOL. *Multiphysics v. 6.2*; COMSOL AB: Stockholm, Sweden, 2024. www.comsol.com.
(36) Boschi, A.; Gebeyehu, Z. M.; Slizovskiy, S.; Mišeikis, V.; Forti, S.; Rossi, A.; Watanabe, K.; Taniguchi, T.; Beltram, F.; Fal'ko, V. I.; Coletti, C.; Pezzini, S. Built-in Bernal gap in large-angle-twisted monolayer-bilayer graphene. *arXiv:2406.04732v1*. DOI: 10.48550/arXiv.2406.04732.
(37) Slizovskiy, S.; Garcia-Ruiz, A.; Berdyugin, A. I.; Xin, N.; Taniguchi, T.; Watanabe, K.; Geim, A. K.; Drummond, N. G.; Fal'ko, V. I. Out-of-Plane Dielectric Susceptibility of Graphene in Twistronic and Bernal Bilayers. *Nano Lett.* **2021**, *21*, 6678.
(38) Icking, E.; Banszerus, L.; Wörtche, F.; Volmer, F.; Schmidt, P.; Steiner, C.; Engels, S.; Hesselmann, J.; Goldsche, M.; Watanabe, K.; Taniguchi, T.; Volk, C.; Beschoten, B.; Stampfer, C. Transport Spectroscopy of Ultraclean Tunable Band Gaps in Bilayer Graphene. *Adv. Electron. Mater.* **2022**, *8*, 2200510.
(39) Balandin, A. A. Low-frequency 1/f noise in graphene devices. *Nat. Nanotechnol.* **2013**, *8*, 549−555.
(40) Javadi, E.; But, D. B.; Ikamas, K.; Zdanevičius, J.; Knap, W.; Lisauskas, A. Sensitivity of Field-Effect Transistor-Based Terahertz Detectors. *Sensors* **2021**, *21*, 2909.
(41) Asgari, M.; Coquillat, D.; Menichetti, G.; Zannier, V.; Dyakonova, N.; Knap, W.; Sorba, L.; Viti, L.; Vitiello, M. S. Quantum-Dot Single-Electron Transistors as Thermoelectric Quantum Detectors at Terahertz Frequencies. *Nano Lett.* **2021**, *21*, 8587−8594.

https://doi.org/10.1021/acs.nanolett.4c04934
Nano Lett. 2025, 25, 6005−6012

(42) Viti, L.; Cadore, A. R.; Yang, X.; Vorobiev, A.; Muench, J. E.; Watanabe, K.; Taniguchi, T.; Stake, J.; Ferrari, A. C.; Vitiello, M. S. Thermoelectric graphene photodetectors with sub-nanosecond response times at terahertz frequencies. *Nanophotonics* **2020**, *10*, 89−98.
(43) Bandurin, D. A.; Svintsov, D.; Gayduchenko, I.; Xu, S. G.; Principi, A.; Moskotin, M.; Tretyakov, I.; Yagodkin, D.; Zhukov, S.; Taniguchi, T.; Watanabe, K.; Grigorieva, I. V.; Polini, M.; Goltsman, G. N.; Geim, A. K.; Fedorov, G. Resonant terahertz detection using graphene plasmons. *Nat. Commun.* **2018**, *9*, 5392.
(44) Caridad, J. M.; Castelló, Ó.; López Baptista, S. M.; Taniguchi, T.; Watanabe, K.; Roskos, H. G.; Delgado-Notario, J. A. Room-Temperature Plasmon-Assisted Resonant THz Detection in Single-Layer Graphene Transistors. *Nano Lett.* **2024**, *24*, 935−942.
(45) Asgari, M.; Viti, L.; Balci, O.; Shinde, S. M.; Zhang, J.; Ramezani, H.; Sharma, S.; Meersha, A.; Menichetti, G.; McAleese, C.; Conran, B.; Wang, X.; Tomadin, A.; Ferrari, A. C.; Vitiello, M. S. Terahertz photodetection in scalable single-layer-graphene and hexagonal boron nitride heterostructures. *Appl. Phys. Lett.* **2022**, *121*, No. 031103.

https://doi.org/10.1021/acs.nanolett.4c04934
Nano Lett. 2025, 25, 6005−6012